SECONDARY FLOWS INDUCED BY SPANWISE HETEROGENEOUS ROUGH WALLS

Marco Placidi
Department of Mechanical Eng. Sciences
University of Surrey
Guildford, Surrey GU2 7XH
m.placidi@surrey.ac.uk

Takfarinas Medjnoun
Aerodynamics and Flight Mechanics
University of Southampton
Highfield, Southampton, SO17 1BJ, UK
tm1y13@soton.ac.uk

Manuel Aguiar Ferreira
Aerodynamics and Flight Mechanics
University of Southampton
Highfield, Southampton, SO17 1BJ, UK
m.ferreira@soton.ac.uk

Bharathram Ganapathisubramani
Aerodynamics and Flight Mechanics
University of Southampton
Highfield, Southampton, SO17 1BJ, UK
g.bharath@soton.ac.uk

ABSTRACT

Wind tunnel experiments were conducted on rough wall boundary layers developing over surfaces characterised by heterogeneous roughness with the aim of investigating the presence and strength of Prandtl's secondary flows of the second kind. The surfaces investigated herein are created by employing spanwise periodic alternating strips of different grit sandpaper (i.e. variation in the equivalent sand-grain height, k_s). These were adopted with a fixed spanwise wavelength, whilst systematically varying the ratios of the width of coarse/fine sandpaper. Velocity and skin friction drag measurements are obtained via three-dimensional Stereoscopic Particle Image Velocimetry and floating-element force balance, respectively. Evidence is shown for the presence of SFs for all three cases considered. The strength of the mean flow modulation is found to be linked to the underlying surface morphology, and appear to be more affected by a sudden increase in the wall shear stress in the spanwise direction than to a decrease of the same quantity. The location of the high- and low-momentum pathways was found to be consistent with k_s-born SFs in previous literature. Finally, results also indicated that both the mean velocity profiles (in defect form) and the streamwise velocity fluctuations (in the the diagnostic form) conform to outer-layer similarity.

INTRODUCTION AND BACKGROUND

Prandtl recognised the potential existence of secondary flows (SFs) within turbulent boundary layers and attributed those to the non-homogeneity and anisotropy of turbulence (Prandtl's SFs of the second kind). The last decade has seen a renewed interest in these flows, as a number of heterogeneous surfaces have been found, perhaps counterintuitively, to promote significant SFs. These include surfaces characterised by converging-diverging riblets (Nugroho *et al.*, 2013; Kevin *et al.*, 2017), sandpaper roughness (Bai *et al.*, 2018), urban roughness (Vanderwel *et al.*, 2019; Vanderwel & Ganapathisubramani, 2015; Medjnoun *et al.*, 2018; Yang, 2016; Cheng & Castro, 2002; Yang & Anderson, 2018), uneven wear (Barros & Christensen, 2014; Anderson *et al.*, 2015; Mejia-Alvarez & Christensen, 2013), variations in the wall shear stress (Chung *et al.*, 2018; Willingham *et al.*, 2014), and natural river beds (Wang & Cheng, 2006). Therefore, it is paramount to further our understanding of these surface-induced motions. This study is limited to SFs that develop over spanwise heterogeneous surfaces; these induce localised streamwise vorticity, and in turn, coherent pathways of high and low momentum (HMP and LMP).

A classification of these studies is here proposed based on the type of forcing that the surface morphology imposes on the flow and its response. For walls with alternating high and low roughness (i.e. equivalent sand-grain height, k_s) a downwelling motion is induced over the rougher patch due to the increased surface stress, generating HMP, while smoother areas result in LMP (Barros & Christensen, 2014; Anderson *et al.*, 2015; Mejia-Alvarez & Christensen, 2013; Chung *et al.*, 2018; Willingham *et al.*, 2014). Contrarily, for surfaces with severe spanwise discontinuity in the surface elevation (i.e. k) the flow tends to channel in the canyons, as it is not impeded by the rough elements, and therefore, high- and low-momentum regions line up with valleys and peaks, respectively (Vanderwel & Ganapathisubramani, 2015; Medjnoun *et al.*, 2018; Yang, 2016). This simple physical interpretation of the effect of spanwise periodic surface elevation or surface roughness, and hence of the direction of the induced SFs, is conceptually represented in figure 1. This classification has found to reconcile most of the previous studies described so far. Interesting cases, however, are represented by surfaces with a small spanwise gradient in the surface elevation, which show inconsistency in the locations of the HMPs (Yang & Anderson, 2018; Awasthi & Anderson, 2018). The roughness and the surface elevation appear to be competing effects, and the dominance of one over the other depends on a number of additional parameters, which need to be further explored.

Here, we attempt to eliminate the surface elevation from the parameter space, by employing surfaces with spanwise variation in roughness (i.e. k_s), while minimising the discontinuity in height (k). Three different surfaces were

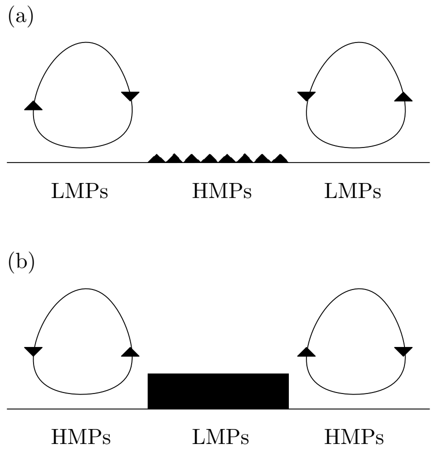

Figure 1. Classification of secondary flows based on surface morphology over which they originate. (a) alternating surfaces with high and low roughness; (b) alternating surfaces with elevation discontinuity.

considered to systematically investigate (i) the presence and strength of SFs, and (ii) the location of the HMPs as a function of the coarse to fine sandpaper width ratio, w_c/w_f, whilst keeping the wavelength of the heterogeneity, S, fixed. To the best of the authors' knowledge, this has not been attempted before.

METHODOLOGY AND DETAILS

Roughness morphology

The morphologies adopted in this work were generated by alternating strips of different grit sandpaper mounted on wooden boards. The boards were installed so that the roughness strips were perfectly aligned with the tunnel walls by using a Stanley Cubix Self-Levelling Cross Line Laser. The sandpaper was Norton Aluminium Oxide Very Fine Abrasive Cloth Roll (240 Grit), and Norton Aluminium Oxide Coarse Abrasive Cloth Roll (40 Grit). These were arranged in the three different configurations by keeping the repeating spanwise wavelength fixed to $S = 100$ *mm* while varying the width covered by coarse and fine sandpaper, w_c and w_f respectively, as shown in figure 2.

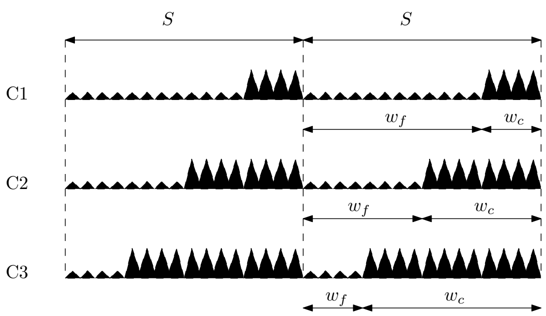

Figure 2. Sketch of test cases. Elevation gradients, $\partial k/\partial z$, have been enhanced for clarity (i.e. not in scale).

The cases are summarised in Table 1. The employment of sandpaper was chosen to remove the surface elevation variable from the parameter space, as the difference in height between the two grits was limited to below 1 *mm*. The flow was left to develop over the roughnesses for over 3 *m* before the measurements were taken; this represented more than 40 δ. The incoming wind was lifted up to the top of the roughness by an aluminium ramp angled at approximately 2.5°, to allow for a gentle flow development.

Table 1. Summary of test cases. Measurements are in *mm*.

Case	Symbol	w_c	w_f	S	S/δ	Re_τ
C1	△	25	75	100	1.57	≈ 3200
C2	○	50	50	100	1.39	≈ 3800
C3	□	75	25	100	1.37	≈ 4300

Experimental Facility

The current experiments were carried out in the suction wind tunnel within the experimental fluid mechanics laboratory at the University of Southampton. The tunnel has a working section of 4.5 *m* in length, with a 0.9 $m \times 0.6$ *m* cross-section. The free-stream turbulence intensity is adequately low for the purpose of this work ($Tu < 0.3\%$), and homogeneous in the test section. The streamwise, wall-normal and spanwise directions are named $x - y - z$ with respective instantaneous velocity components $u - v - w$. Time-averaged velocities are capitalised, while the turbulent fluctuations are denoted with a $'$. All the tests were conducted at a nominal velocity of 23 ms^{-1}, measured by a Pitot-static tube in the tunnel test section, and in nominally zero-pressure-gradient conditions.

Experimental techniques

Particle image Velocimetry Measurements were taken 3.1 *m* downstream of the start of the roughness. Vector fields were acquired using Stereo Particle Image Velocimetry (SPIV) in a cross-plane (i.e. $y - z$) roughly in the tunnel centreline. The Field of View (FOV) was approximately 120×200 mm^2 ($y \times z$), which included two complete spanwise wavelengths and extended well into the freestream in the wall-normal direction. The flow was seeded with vaporised glycol-water solution particles (1 μm in diameter) illuminated with a 1 *mm* thick laser sheet produced by a pulsed Litron Nano Nd:YAG Laser (200 *mJ*). Two Imager LX 16 *M pixel* cameras equipped with 300 *mm* Nikon lenses, at $f/4$, were used to capture the flow field. Sets of 2000 image pairs were captured at 0.5 *Hz* for each test case, and post-processed with DaVis 8.0 software. Velocity vectors were obtained using a multi-pass scheme down to 24×24 $pixel^2$ interrogation windows with 50% overlap. This resulted in a vector spacing of 0.92×0.92 mm^2.

Floating element force balance The drag generated by the different wall morphologies was directly measured via a floating-element force balance. This innovative design is described in detail in Aguiar Ferreira *et al.* (2018). The floating element was located approximately centred around the SPIV measurements at circa 3 *m* downstream along the test section. A 200×200 mm^2 coupon covered with the testing surfaces was positioned in the tunnel floor through a cut hole mechanically mounted on the floating element of the balance. A 1 *mm* gap was present around the coupon to allow for free floatation of the element. The size of the floating element was such that two complete roughness wavelengths were contained within the measuring coupon. Preliminary analysis of the results of these direct measurements suggests a non-negligible contribution of the loads acting on the lip of the floating element to the drag, which amplifies the effect of the small, yet present, streamwise pressure gradient in the wind tunnel and the pressure difference induced by the flow through the gap around the floating element. This was due to a design fault within the floating element roughness tile used in this particular experiment which has, since, been rectified. It is yet unclear whether these direct drag measurements are reliable or whether they should be repeated. Therefore, in this study we use the total stress method based on the plateaux in the Reynolds shear stresses to calculate the skin friction drag (Amir & Castro, 2011; Vanderwel & Ganapathisubramani, 2015).

PRELIMINARY RESULTS

Two-dimensional contour plots

Preliminary results were obtained by processing a small batch of digital images for each case. These seem largely converged. Figure 3 shows contours of non-dimensional streamwise velocity profiles for C1, C2, and C3 cases, on the top, centre, and bottom, respectively. These vector fields are taken in a cross-plane ($y-z$), approximately 40δ downstream of the start of the roughness. We also included in the figure, the location of the coarse and fine sandpaper strips. It should be noted that the C1 case in figure 3(a) was affected by a severe light reflection in the near wall region, which invalidated the data points within this area. These are, therefore, not included in the analysis. Additional data have been acquired after having minimised the laser reflection by covering the rough surfaces with matt black paint. This data is not presented herein as it is still currently been post-processed. It is confirmed that all morphologies behave as spanwise heterogeneous surfaces, as the mean flow is highly modulated by the features of the underlying wall. This modulation is a typical manifestation of Prandtl's SFs of the second kind, and is qualitatively in line with previous numerical and experimental work on surfaces characterised by a spanwise discontinuity in wall shear stress (Chung *et al.*, 2018; Willingham *et al.*, 2014; Bai *et al.*, 2018). Also in line with previous work on similar surfaces is the location of the high- and low-momentum pathways. These are found to be aligned with the coarser (40 grit) and smoother (240 grit) roughness strips, respectively, in line with the phenomena described in the introduction of this paper. Interestingly, different degrees or strengths of the mean flow modulation are shown across the three different cases, in line with the aims and research question of this paper.

Qualitatively, it appears that the strength of the secondary flows is inversely proportional to the ratio of the coarse to fine sandpaper widths, w_c/w_f. This could be an indication that either (a) these secondary motions are more susceptible to a sudden increase in the wall shear stress in the spanwise direction than they are to a decrease of the same quantity (at a fixed magnitude) or (b) that this effect is purely due to the minute - yet present - discontinuity in surface elevation across the sandpaper strips of different grit. The latter explanation, however, seems unlikely given that the distribution of the high- and low- momentum pathways are in accordance with k_s-born SFs (as discussed in the introduction), and that the difference in elevation between the two surfaces is below 1 *mm*. Also of importance seems to be the width of the coarser roughness as the flow needs a certain "fetch" to adjust to the spanwise gradient in wall shear stress.

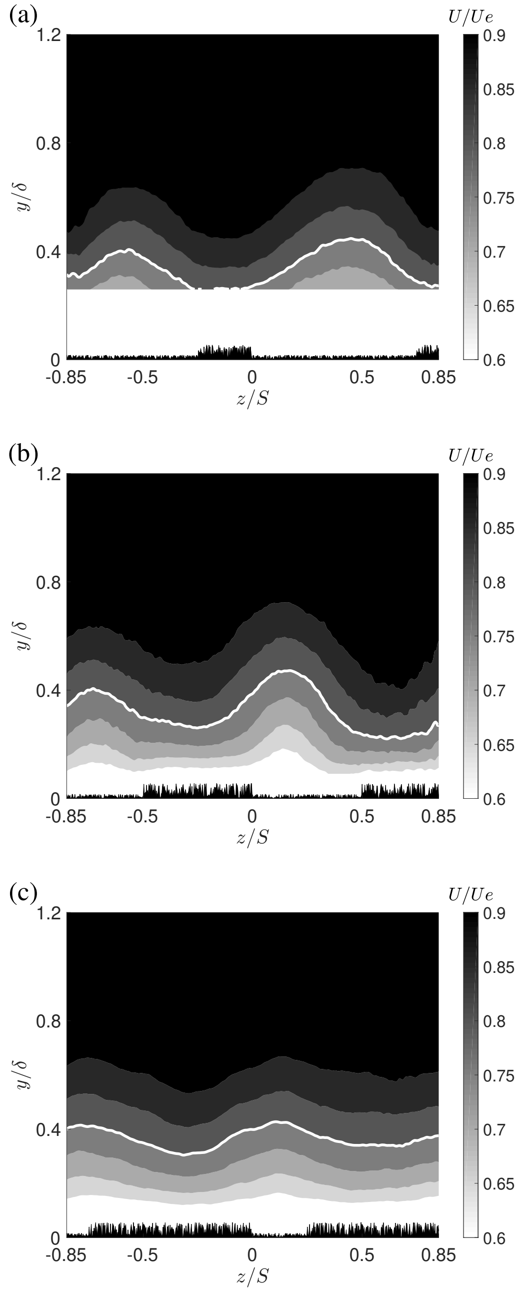

Figure 3. Contours of non-dimensional mean streamwise velocity, U/U_∞, over the tree surface roughnesses.(a) C1, (b) C2 and (c) C3. The location of the surface roughness is also reported where its wall normal extent has been enhanced for visualisation purposes. Contour for $U/U_\infty = 0.8$ are also reported in white to highlight the mean flow modulation.

To further explore the structure of the secondary flows, an example of the transverse turbulent stresses is also shown in figure 4, where the particularly significant $u'w'$ product is compared across all the roughness cases. These are clearly found to be largely periodic and symmetric for all cases, in accordance with the spanwise variation in the surface underneath, which dictates the directionality of the SFs. These findings are in agreement with those contained in Anderson *et al.* (2015). Similar conclusions can be drawn by exploring maps of $v'w'$, omitted here for the sake of brevity. Also noticeable is the strength of the transverse stress across the surfaces. This correlates well with the severity of the SFs and their effect on the modulation of the mean velocity (previously shown in figure 3). Here, it appears that C1 and C2 display the strongest SFs, while case C3 shows the weakest. To be noted that the near-wall region for the C1 case was not appropriately resolved, which makes it is difficult to conclusively discuss this case - however, qualitatively this seems to align with case C2. Also of note for case C1 is the location of the positive and negative lobes, which appears to be slightly shifted in respect of the overlying texture when compared to the other two cases - this is consistent with the location of peaks and valleys in the mean velocity profiles (see figure 3), however it requires further investigation.

One-dimensional velocity profiles

It was shown in the previous section (particularly in figure 3) that a significant extent of the wall-normal range is influenced by the SFs, therefore, their effect on the self-similar characteristics of the mean velocity profiles is an important aspect to be addressed. This is explored in this section which presents one-dimensional profiles spatially averaged across on roughness wavelength. The mean velocity profiles are shown in figure 5.

All rough surfaces appear to show a reasonable collapse in the outer region, however, as highlighted in Vanderwel & Ganapathisubramani (2015) closer to the wall the ratio of the roughness wavelength to the boundary layer thickness becomes an important discriminant. Here the case C1 sits just below the other two in accordance with its "coarser" spanwise roughness spacing as reported in table 1. Here, the term "coarse" is used in accordance with the definition in Vanderwel & Ganapathisubramani (2015). Next, the characteristics of the streamwise velocity fluctuations are considered. Given the high degree of heterogeneity of these rough surfaces - and hence of the local skin friction (Medjnoun *et al.*, 2018) - the most appropriate approach to address the validity of Townsend's similarity hypothesis (Townsend, 1976) is by means of diagnostic plot, which eliminates the need to define an appropriate scaling (Alfredsson & Örlü, 2010). This is shown in figure 6. The three surfaces show a good collapse over the entire wall-normal range in investigation, which suggests the validity of outer-layer similarity for the streamwise velocity fluctuations. The data does not, however, conform to the fully-rough asymptote proposed by Castro *et al.* (2013), despite the relatively high roughness Reynolds number (shown in table 1). This is believed to be due to (i) the presence of the SFs and (ii) the fact that this asymptote was obtained mostly based on rough wall datasets characterised by severe roughness.

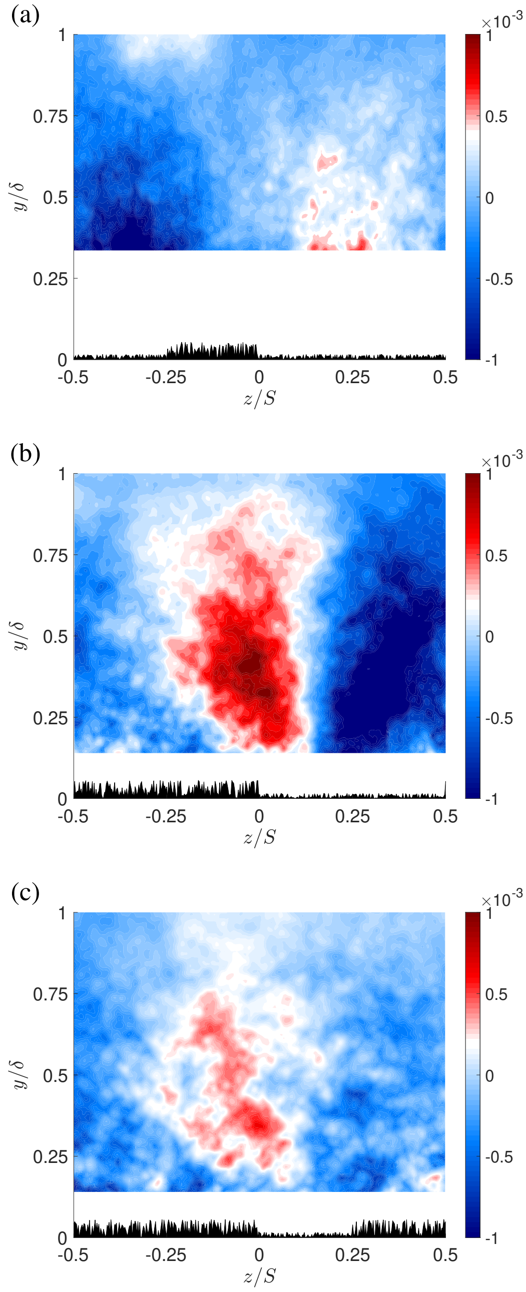

Figure 4. Contours of non-dimensional turbulent stresses, $u'w'/U_\infty{}^2$, across one roughness wavelength for the tree surface roughnesses.(*a*) C1, (*b*) C2 and (*c*) C3. The location of the surface roughness is also reported where its wall normal extent has been enhanced for visualisation purposes.

CONCLUSIONS AND FUTURE WORK

Wind tunnel tests were conducted on alternating strips of different grit sandpaper to investigate the formation mechanism of Prandtl's secondary flows of the second kind. These sandpaper strips were adopted with a fixed spanwise wavelength while modifying the ratios of the width of coarse/fine sandpaper. Stereoscopic PIV and direct force measurements are employed in this work. SFs were found to be present and significant for all the surfaces tested herein. Their strength appeared to be more affected by a sudden increase rather than a decrease in the wall shear stress in the spanwise direction. The location of the upwelling/downwelling was found to align with strips of low and high roughness respectively, in accordance with previous work on similar roughness types (Barros & Christensen, 2014; Anderson *et al.*, 2015; Mejia-Alvarez & Christensen, 2013; Chung *et al.*, 2018; Willingham *et al.*, 2014). Finally, results indicated a good collapse of the mean and fluctuating velocity profiles in the streamwise direction, which

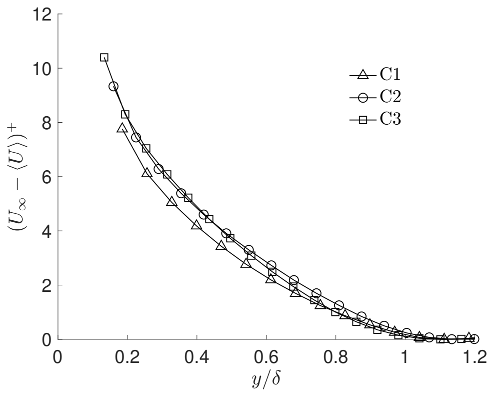

Figure 5. Profiles of defect mean velocity profiles averaged across one roughness wavelength for the different rough surfaces. Markers are spaced every 10 data points for clarity.

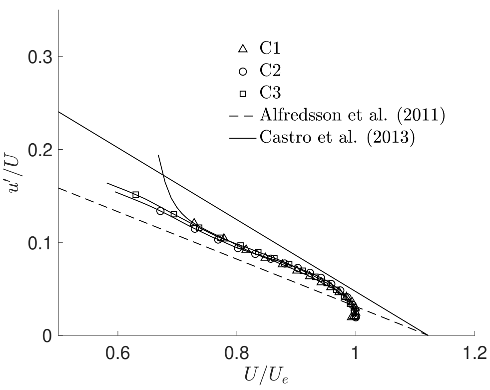

Figure 6. Diagnostic plot for the different rough surfaces. The black solid line represents the fully-rough asymptote from Castro *et al.* (2013), while the dashed line is the smooth-wall asymptote, as in Alfredsson *et al.* (2011). Markers are spaced every 10 data points for clarity.

points toward the validity of outer-layer similarity hypothesis. It should be noted that the analysis described herein is only preliminary and has been conducted on a limited subset of the available data. These are still being investigated. Further work aims to explore the role of SFs via means of quadrant analysis and proper orthogonal decomposition.

REFERENCES

Aguiar Ferreira, Manuel, Rodriguez-Lopez, E & Ganapathisubramani, Bharathram 2018 An alternative floating element design for skin-friction measurement of turbulent wall flows. *Experiments in Fluids* **59**, 1–14.

Alfredsson, Henrik P & Örlü, Ramis 2010 The diagnostic plot — a litmus test for wall bounded turbulence data. *European Journal of Mechanics - B/Fluids* **29** (6), 403–406.

Alfredsson, Henrik P, Segalini, Antonio & Örlü, Ramis 2011 A new scaling for the streamwise turbulence intensity in wall-bounded turbulent flows and what it tells us about the "outer" peak. *Physics of Fluids* **23** (4), 041702.

Amir, Mohammad & Castro, Ian P 2011 Turbulence in rough-wall boundary layers: universality issues. *Experiments in Fluids* **51**, 313–326.

Anderson, William, Barros, Julio M, Christensen, Kenneth T & Awasthi, Ankit 2015 Numerical and experimental study of mechanisms responsible for turbulent secondary flows in boundary layer flows over spanwise heterogeneous roughness. *Journal of Fluid Mechanics* **768**, 316–347.

Awasthi, Ankit & Anderson, William 2018 Numerical study of turbulent channel flow perturbed by spanwise topographic heterogeneity: Amplitude and frequency modulation within low- and high-momentum pathways. *Physical Review Fluids* p. 044602.

Bai, H L, Kevin, Hutchins, Nicholas & Monty, Jason P 2018 Turbulence modifications in a turbulent boundary layer over a rough wall with spanwise-alternating roughness strips. *Physics of Fluids* **30** (5), 055105–18.

Barros, Julio M & Christensen, Kenneth T 2014 Observations of turbulent secondary flows in a rough-wall boundary layer. *Journal of Fluid Mechanics* **748**, R1.

Castro, Ian P, Segalini, Antonio & Alfredsson, Henrik P 2013 Outer-layer turbulence intensities in smooth- and rough-wall boundary layers. *Journal of Fluid Mechanics* **727**, 119–131.

Cheng, H & Castro, Ian P 2002 Near wall flow over urban-like roughness. *Boundary-Layer Meteorology* **104**, 411–432.

Chung, D, Monty, Jason P & Hutchins, Nicholas 2018 Similarity and structure of wall turbulence with lateral wall shear stress variations. *Journal of Fluid Mechanics* **847**, 591–613.

Kevin, Kevin, Monty, Jason P, Bai, H L, Pathikonda, G, Nugroho, B, Barros, Julio M, Christensen, Kenneth T & Hutchins, Nicholas 2017 Cross-stream stereoscopic particle image velocimetry of a modified turbulent boundary layer over directional surface pattern. *Journal of Fluid Mechanics* **813**, 412–435.

Medjnoun, Tak, Vanderwel, Christina & Ganapathisubramani, Bharathram 2018 Characteristics of turbulent boundary layers over smooth surfaces with spanwise heterogeneities. *Journal of Fluid Mechanics* **838**, 516–543.

Mejia-Alvarez, R & Christensen, Kenneth T 2013 Wall-parallel stereo particle-image velocimetry measurements in the roughness sublayer of turbulent flow overlying highly irregular roughness. *Physics of Fluids* **25** (11), 115109.

Nugroho, B, Hutchins, Nicholas & Monty, Jason P 2013 Large-scale spanwise periodicity in a turbulent boundary layer induced by highly ordered and directional surface roughness. *International Journal of Heat and Fluid Flow* **41** (C), 90–102.

Townsend, A A 1976 *The structure of turbulent shear flow*. Cambridge University Press, Cambridge.

Vanderwel, Christina & Ganapathisubramani, Bharathram 2015 Effects of spanwise spacing on large-scale secondary flows in rough-wall turbulent boundary layers. *Journal of Fluid Mechanics* **774**, R2–2–12.

Vanderwel, Christina, Stroh, A, Kriegseis, J, Frohnapfel, B & Ganapathisubramani, Bharathram 2019 The instantaneous structure of secondary flows in turbulent boundary layers. *Journal of Fluid Mechanics* **862**, 845–870.

Wang, Zhi-Qian & Cheng, Nian-Sheng 2006 Time-mean structure of secondary flows in open channel with longitudinal bedforms. *Advances in Water Resources* **29** (11), 1634–1649.

Willingham, David, Anderson, William, Christensen, Kenneth T & Barros, Julio M 2014 Turbulent boundary layer flow over transverse aerodynamic roughness transitions: Induced mixing and flow characterization. *Physics of Fluids* **26** (2), 025111.

Yang, Jianzhi & Anderson, William 2018 Numerical Study of Turbulent Channel Flow over Surfaces with Variable Spanwise Heterogeneities: Topographically-driven Secondary Flows Affect Outer-layer Similarity of Turbulent Length Scales. *Flow Turbulence Combust* **100**, 1–17.

Yang, Xiang I A 2016 On the Mean Flow Behaviour in the Presence of Regional-Scale Surface Roughness Heterogeneity. *Boundary-Layer Meteorology* **161** (1), 127–143.